Vortex Filament Simulation of the Turbulent Boundary Layer

Peter S. Bernard*
University of Maryland, College Park, Maryland 20742
and
Pat Collins† and Mark Potts‡
VorCat, Inc., North Potomac, Maryland 20878

DOI: 10.2514/1.J050224

A hybrid vortex filament scheme with the capability of simulating bounded turbulent flows is described. Viscous generation of new vortex elements at solid surfaces is accomplished through the intermediary step of solving the viscous vorticity transport equation on a thin boundary mesh via a finite difference and finite volume method. The transitional and turbulent boundary-layer flow past a wide, finite thickness, flat plate with rounded edges is computed with a view toward validating the methodology and gaining new insight into the structural aspects of transition. The predicted mean velocity and related statistics are well matched to experimental and numerical data. The representation of the flow through vortex filaments reveals that a distinction needs to be made between vortical structures, on one hand, and the rotational motion that they produce in the flowfield, on the other hand. In particular, hairpin-shaped regions that are commonly found by vortex identification schemes are found to not be structures in their own right, but rather the rotational signature of raised furrows in the surface vortex sheet. The latter overlie low-speed streaks and evolve to include ejected mushroom-shaped structures as well as spanwise vortices associated with roll-up.

Nomenclature

C_f	=	local skin-friction coefficient
c_f	=	drag coefficient
M	=	number of wall-normal grid levels
L_T	=	average triangle edge length
R_e	=	Reynolds number
$\mathbf{s}$	=	axial vector on vortex tube
U, u	=	streamwise velocity and fluctuation
U_i	=	velocity vector
U_τ	=	friction velocity
U_∞	=	far-field velocity
V, v	=	wall-normal velocity and fluctuation
V_T	=	prism volume
W, w	=	spanwise velocity and fluctuation
x	=	streamwise coordinate
y	=	wall-normal coordinate
z	=	spanwise coordinate
Γ	=	circulation
δ	=	displacement thickness
η	=	similarity variable
θ	=	momentum thickness
σ	=	smoothing parameter
ϕ	=	smoothing function
Ω_i	=	vorticity vector

Superscript

$+$	=	wall variables

I. Introduction

BELIEVING that it may be advantageous to represent turbulent flow numerically via grid-free vortex filaments is a natural response to the highly rotational character of turbulence that includes, at one extreme, small-scale wormlike vortices and, at the other extreme, well-organized vortices associated with the flow origins [1]. The recognition of the central importance of vortex dynamics to understanding turbulent physics is also implicit in the many studies that seek to extract vortex structure from computed velocity fields [2] or even go so far as to reconstruct from the velocity field the time-dependent behavior of the vortical structures [3]. Such analyses (which are inherently difficult for traditional grid-based schemes) are straightforward for the vortex filament approach, since the vortex dynamics are provided directly.

As in grid-based simulations of turbulence, it is not generally practical to represent the full range of scales with a filament scheme, so that the most useful context for such an approach is as a large eddy simulation (LES), in which the effects of small, invisible, subgrid motions on the resolved are modeled. Recent applications of such a grid-free LES method to turbulent free shear flows including the mixing layer [4] and round coflowing jet [5] have demonstrated some of the advantages of the approach. The present work is concerned with the implementation of this idea in the more general context of flows containing solid walls with a primary focus on the turbulent boundary layer.

In traditional grid-based LES, each vortex of resolvable scale that appears in the simulated flowfield requires a collection of individual mesh points in its representation. The same vortex is generally more efficiently resolved in terms of vortex elements, though a potentially more significant advantage of a filament scheme is that without a mesh, flow features that otherwise may be smeared by numerical diffusion [6,7] remain sharply defined. In the context of an LES, it is also necessary to provide a subgrid-scale model that acts as a gatekeeper for two-way energy transfer between small dissipative scales and large resolved scales. Primarily for reasons having to do with numerical stability, subgrid models used in grid-based schemes [8] tend to rely on diffusive models that have the potential to distort important vortical flow features as well as inhibit local backscatter. In contrast, the vortex filament method relies on a nondiffusive vortex loop-removal algorithm [9–11] that accounts for local energy dissipation without compromising the sharpness of coherent vortical structures or hindering the passage of energy from small to large scales.

Whatever advantages vortex filaments might have in representing turbulence structure, this is lost in the region flush against solid boundaries, within which the vorticity field acquires in part a largely

Received 19 September 2009; revision received 28 January 2010; accepted for publication 12 March 2010.

*Professor, Department of Mechanical Engineering. Member AIAA.
†Senior Research Scientist. Member AIAA.
‡Senior Research Scientist.

two-dimensional sheetlike character. In fact, gradients in the vorticity field at the wall surface control viscous production of vorticity, and it is unlikely that tubelike elements even in prodigious numbers can do justice to the accurate representation of this type of field. It is also well known that essentially all scales of motion next to a wall need to be resolved, since no part of the motion can be safely considered subgrid and suitable for modeling. These considerations motivate the belief that if the filament scheme is to be extended to include solid boundaries, then it must be done so in such a way that the near-wall vorticity field (specifically, that part within which viscous production of new vorticity takes place) is simulated with the resolution and accuracy of a conventional direct numerical simulation (DNS).

In this paper, a hybrid scheme is described that combines the vortex filament representation of the flow outside the immediate vicinity of walls, with a finite volume and finite difference algorithm applied to the solution of the full three-dimensional viscous vorticity equation on a thin mesh situated against bounding solid surfaces. New filaments appear in the flow at the outer edge of the near-wall mesh. The latter is limited in thickness to the extent necessary to well represent near-wall viscous vorticity diffusion. In practice, the wall mesh is erected from a surface triangularization maintaining a sheetlike aspect ratio to the prism elements and thus avoids many of the complexities normally associated with three-dimensional mesh development.

The turbulent boundary layer is treated here as an important step in validating the vortex filament methodology in the presence of solid walls. At the same time it will be seen that the vortex calculations offer a novel viewpoint with which to examine the physics of the boundary layer and, from so doing, arrive at new understanding of some of its essential features. A case in point will be the opportunity to take a more holistic view of the vortical field during transition than has been normally possible, and from this refine our understanding of the origin, meaning, and behavior of previously noted vortical features.

Because of its fundamental nature, the boundary layer (both transitional and fully turbulent) has been the object of many previous numerical studies involving both DNS and LES. Among the first DNS calculations, Spalart [12] accounted for spatial growth via a mapping technique so as to enable the use of a spectral scheme with streamwise periodic boundary conditions. This study produced well-documented averaged flow data for the turbulent boundary layer at several Reynolds numbers that are helpful for validating the present calculations. In an early study, the spatially growing boundary layer was treated directly by Rai and Moin [13] using a zonal finite difference approach. They computed the boundary-layer transition into the turbulent regime. Many subsequent DNS studies of the spatially developing boundary layer have focused on the transitional case in which a variety of different modes of the process have been investigated. Among these, Rist and Fasel [14] studied the evolution of controlled disturbances and gained insights into the growth and breakup of vortical structures. Jacobs and Durbin [15] simulated bypass transition in a spatially growing boundary layer excited by freestream turbulence. They examined the origins of low-speed streaks and their association with the mechanisms causing the appearance of turbulent spots. The dynamics of the so-called Klebanoff transition were studied via matched experiments and DNS by Bake et al. [16]. A detailed scenario was developed connecting the onset of random disturbances in the boundary layer with the growth and evolution of vortical structures. Ovchinnikov et al. [17] computed the effect of large-amplitude freestream turbulence on the transitional boundary layer, noting circumstances when the breakdown of low-speed streaks occurs vs the appearance of turbulent spots. Recently, Wu and Moin [18] computed the spatially growing boundary layer through transition and well into the turbulent realm. A primary focus of this work is concerned with demonstrating that vortical structures in the form of hairpin packets [19] play a dominant role as a structural element throughout all aspects of the boundary layer from transition onward.

Within the realm of LES techniques there has also been some significant work devoted to studying boundary layers. These studies tend to require the use of specially adapted subgrid models in order to accommodate the presence of transition. For example, Ducros et al. [20] simulated a forced, narrow, Mach 0.5 boundary layer through transition to turbulence using a subgrid model that allows for weak perturbations without overly dissipating the turbulent field. They were able to qualitatively describe some aspects of transition into turbulence. The turbulent region of the flow retained structural features such as streaks and bursting that are commonly observed in other simulations. Another application of LES to boundary-layer modeling in the compressible regime was performed by Kawai and Fujii [21], in which the effects of numerical and modeling parameters on the physicality of the transitional and turbulent structure were explored.

Despite the unorthodoxy of the vortex filament representation of the boundary layer used in the present study, it will be clear below that the statistical measures of the computed field in terms of mean velocity and other properties show considerable conformity to that found in traditional studies. Moreover, it will be seen that a connection can be made between the physical appearance of the filament field and the coherent vortical objects that have played a major role in categorizing the dynamical processes at work in the boundary layer: both transitional and turbulent. It is through this connection (which does not require the use of a vortex identification procedure as an intermediary) that an opportunity arrives to acquire new insights into the physics of the boundary layer.

The hybrid vortex filament approach will be described in the next section with an emphasis on the finite volume and finite difference algorithm. This is followed by a discussion of the numerical problem to be considered with subsequent sections describing the quantitative and structural aspects of the predicted results for transitional and turbulent boundary layers. Finally, some conclusions are drawn.

II. Numerical Method

Various aspects of the numerical simulation technique are now described with the greatest emphasis placed on the near-wall treatment. Additional information about the vortex filament methodology can be found in the literature [4,5,9].

A. Vortex Tubes

The vortex filament method uses short, straight, vortex tubes linked end-to-end forming filaments as the basic computational element. Vortex tubes that stretch beyond a threshold are subdivided. An essential aspect of the technique is the removal of vortex loops that form naturally out of the filaments as the tubes stretch and fold in turbulent flow regions. As first suggested by Chorin [10,11] and demonstrated in applications [4,5,9], this is an effective means of accommodating nonlocal intermittent energy dissipation at inertial range scales without the expense of computing the details of viscous dissipation at much smaller scales. At the same time, loop removal does not hinder the tendency of the vortex filaments to combine forming large scale structures: essentially, the phenomenon of backscatter. Loop removal is also of considerable practical importance, since it prevents what would ordinarily be an exponential growth in the number of tubes produced as a byproduct of the energy cascade to small dissipative scales caused by vortex stretching and folding.

Vortex tubes are introduced into the calculation from vorticity created at solid surfaces as described below. As the vortices stretch the number of tubes increases by subdivision and in turbulent regions their number is controlled via loop removal. It is also necessary to introduce a downstream boundary beyond which vortices are removed from the computation. For the present simulations, entire filaments are removed when each of the component vortices is past the exit plane. As has been mentioned in other contexts [4,5], removal of vorticity outside the computational domain can be expected to have some effect on the flow inside due to the use of the Biot–Savart law in computing velocities. For the present work, this means that a region just upstream of the exit plane will be less accurate and thus not suitable for analysis.

B. Finite Volume and Finite Difference Scheme

To accommodate the need for DNS resolution adjacent to solid boundaries, a fine mesh is constructed from a surface triangularization by erecting perpendiculars at the nodal points. $M-1$ layers of thickness Δy are placed on top of an initial half-thickness layer [22], giving a total thickness of the mesh equal to $(M-1/2)\Delta y$, where y is in the direction normal to the surface and x and z are the tangential coordinates. The flow region covered by triangular prisms is taken to be large enough to encompass the viscous sublayer and adjacent region of the turbulent boundary layer: that part of the flow in which the wall-normal gradients of the vorticity are large. In terms of wall units $y^+ = yU_\tau/\nu$, where the friction velocity $U_\tau \equiv \sqrt{\nu \partial \bar{U}/\partial y(0)}$, the mesh is set to lie approximately within $y^+ = 25$ of the boundary. The precise distance in wall units at the outer edge of the mesh will vary from place to place in any given calculation.

An important consideration is the aspect ratio of the triangular prisms defined as the average edge length divided by the thickness of the prisms. In the interest of efficiency, both to minimize the number of surface elements and to enhance the velocity computation described below, it is advantageous to have the prisms be sheetlike in character: that is, the aspect ratio should not be too small. On the other hand, discretization errors will grow and resolution will be lost if the aspect ratio is too large. Empirical tests suggest a value around 10 is acceptable so that if $M = 10$, then $\Delta y^+ \approx 3$ (with the half-sheet at the wall of thickness $\Delta y^+ = 1.5$) and Δx^+, Δz^+ are no larger than 30. These dimensions are at the upper range of those required for a DNS (most significantly, Δz^+ should be smaller) but prove to be adequate for most aspects of the present simulations as will be seen below.

The vorticity field in the mesh, Ω_i, is determined as a solution to the vorticity transport equation:

$$\frac{\partial \Omega_i}{\partial t} + U_j \frac{\partial \Omega_i}{\partial x_j} = \Omega_j \frac{\partial U_i}{\partial x_j} + \frac{1}{R_e} \nabla^2 \Omega_i \tag{1}$$

where U_i is the velocity field and R_e is the Reynolds number. The finite volume/finite difference scheme is developed based on the properties of triangular prisms such as that shown in Fig. 1. In this, the vorticity is taken to be constant over the prisms and equal to that at the prism center, and the velocity is computed at the top and bottom triangles. The velocity at each of the six nodal corners of the prism is determined via area-weighted averaging of the velocities on the adjacent triangles.

The convection term in Eq. (1) is approximated by first expressing it in the equivalent conservative form,

$$U_j \frac{\partial \Omega_i}{\partial x_j} = \frac{\partial U_j \Omega_i}{\partial x_j} \tag{2}$$

averaging it over the prism, and then applying the divergence theorem, leading to

$$\frac{\partial U_j \Omega_i}{\partial x_j} \approx \frac{1}{V_T} \int_{V_T} \frac{\partial U_j \Omega_i}{\partial x_j} \, \mathrm{d}V = \frac{1}{V_T} \sum_k A^k \Omega_i^k (U_j^k n_j^k) \tag{3}$$

where the sum is over the five faces of the prism, V_T is the prism volume and for the kth face of the prism, A^k is the area, n_j^k is the outward pointing unit normal vector, and Ω_i^k is the vorticity. On the triangular surfaces the velocity needed in the sum is directly available, and on the side surfaces it is computed from averaging the four nodal values.

Ω_i^k on the two triangular faces is determined from the value on the upwind prism. For example, if the velocity on the top face of the prism in Fig. 1 is up, then Ω_i^k is taken from the prism itself. Otherwise, it is taken from the prism lying above it. In the case of the fluxes through the quadrilateral sides of the prism, the vorticity is computed by a linear least square fit of the vorticities in prisms that are contiguous to the prism on the upwind side of the surface on the same and the immediately neighboring levels above and below, plus the one prism on the downwind side. This is illustrated in Fig. 2 for flow from left to right across the indicated plane.

The evaluation of the stretching term in Eq. (1) is done at the center of the prisms so the vorticity appearing in the expression is directly available. The computation of the velocity gradient, $\partial U_i/\partial x_j$, is done following an approach similar to computing the convection term. In this case, the scalar divergence theorem is used to obtain

$$\frac{\partial U_i}{\partial x_j} \approx \frac{1}{V_T} \sum_k A^k U_i^k n_j^k \tag{4}$$

The value of U_i^k on each surface is determined the same way as for the convection term.

The numerical model for the diffusion term in Eq. (1) distinguishes between diffusion normal and parallel to the surface. In particular, the Laplacian is first expressed in a local rectangular Cartesian coordinate system with n in the direction normal to the solid surface and t_1 and t_2 tangent to the surface, giving

$$\nabla^2 \Omega_i = \frac{\partial^2 \Omega_i}{\partial n^2} + \frac{\partial^2 \Omega_i}{\partial t_1^2} + \frac{\partial^2 \Omega_i}{\partial t_2^2} \tag{5}$$

The normal diffusion term in Eq. (5) is evaluated using a standard second-order finite difference formula using the vorticity values at the centers of the prisms. The two tangential terms are computed by differentiation of a polynomial determined by a second-order least-squares fit of the vorticities of prisms located within a given radius (say, r_D) of the prism center and in the layers immediately above and

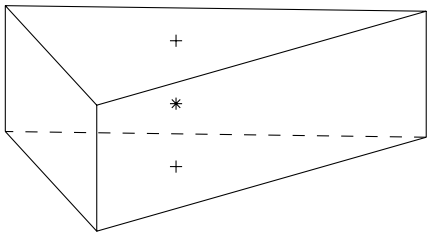

Fig. 1 Typical triangular prism: location of Ω_i (*) and location of computed U_i (+).

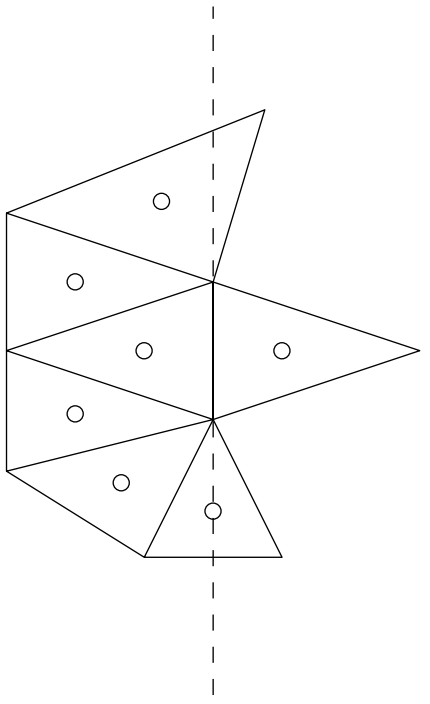

Fig. 2 Example of the prisms used in computing the vorticity convecting through a quadrilateral surface (contained in the dashed line) for the case when flow is from left to right.

below the prism. The default radius is taken to satisfy $r_D = 1.2L_T$, where L_T is the average edge length of the triangles.

As for the accuracy of the discretizations, the upwind advection scheme is nominally first-order in the normal direction and second-order in the horizontal directions. Similarly, the approximation to the stretching term is expected to be essentially second-order. The formula for the Laplacian in the normal direction is second-order and the diffusion scheme in the tangential plane is first-order. With these approximations, the overall scheme offers stable solutions to the 3-D vorticity equation with each separate part being consistent and convergent under mesh refinement.

C. Time Integration

An explicit first-order-in-time Euler scheme is used for advancing the finite volume and finite difference calculation near the wall. In this, the time step Δt is limited by Courant–Friedrichs–Lewy (CFL) conditions in the normal and tangential directions: namely,

$$\Delta t \leq \min(C_{\mathrm{CFL}}\Delta y/V_{\max}, C_{\mathrm{CFL}}L_T/U_{\max}) \tag{6}$$

where C_{CFL} is a parameter usually taken to be 0.3, $V_{\max}$ is the largest wall-normal velocity in the mesh and $U_{\max}$ is the largest tangential velocity. The time step is also limited by a diffusive stability requirement that has

$$\Delta t \leq \frac{R_e}{8}L_T^2 \tag{7}$$

In view of the relatively small size of Δy in comparison to Δx and Δz the condition in the normal direction in Eq. (6) tends to be the strictest. The time step for this part of the calculation is quite small justifying the use of simple explicit time-marching. In practice, Δt satisfying conditions such as Eqs. (6) and (7) is smaller than it would have to be in order to compute accurate motion of the vortex tubes. Consequently, N_S time steps of the wall calculation on the mesh (referred to as subcycles) are performed before updating the positions of the vortex tubes. Typically, $N_S = 10$ and the overall time step in the advancement of the solution is $\Delta t^* = N_S\Delta t$. With this larger time step, a fourth-order Runge–Kutta scheme is used to advance the vortex tubes in time.

D. Boundary Conditions

The vorticity components at the wall surface represent boundary conditions for the computation of vorticity in the mesh. The two tangential vorticity components are approximated from their component velocity derivatives using the divergence theorem to express their average over the half-thickness wall prism in terms of the velocity on the prism faces and the no-slip condition on the wall. The wall-normal vorticity component is identically zero on solid boundaries. In the event that the local boundary element is not aligned with the coordinate system of the calculation, then the wall vorticity components of the latter are determined by projection from those of the former.

To be able to solve for the vorticity in the wall mesh, it is also necessary to have boundary conditions for the vorticity at the top layer of prisms. Moreover, it is required to compute the amount of vorticity that arrives at the top layer to then be turned into new vortex tubes. Both goals are achieved by imposing a zero-net-flux condition on the top layer, in which vorticity entering from the mesh below exits by convection as a new vortex tube. In this there is assumed to be no net gain of vorticity by viscous diffusion at the top sheet level, which is tantamount to assuming that $\partial^2\Omega_i/\partial n^2 = 0$. Moreover, as far as the convective flux between the top two prisms is concerned, when the flux is away from the surface, the vorticity at the top sheet is not needed (in view of the upwind model), and if the flux is toward the surface, it is taken to be zero, since all incoming vorticity is expected to be in the form of vortex tubes.

E. Vortex Creation

Vorticity that accumulates during a prescribed time interval (which may be larger than Δt^*) in the top prism at any location due to the viscous and convective fluxes outward from the wall, is turned into a vortex tube as long as its magnitude is larger than a threshold (0.1 in the present case). This aids computational efficiency by preventing the appearance of many relatively weak vortex filaments. The orientation of the new vortex is clear from the relative magnitudes of the vorticity components. Its midpoint is at the center of the prism whose vorticity it will take. The length of the new tube, $|\mathbf{s}|$, where $\mathbf{s}$ is the axial vector along the tube, is set by the condition that its ends just intersect the sides of the prism. Its strength is determined via the relation

$$\Gamma|\mathbf{s}| = |\boldsymbol{\Omega}|V_T \tag{8}$$

which forces the far-field velocity from the new tube to match that coming from the prism of vorticity it replaces.

F. Velocity Evaluation

The velocity field is computed as the sum of contributions from the vortex elements (both sheets and tubes) as determined from approximations to the Biot–Savart law [23] plus a potential flow given by a boundary element scheme that enforces the nonpenetration boundary condition. The ith vortex tube contributes according to the relation

$$-\frac{1}{4\pi}\frac{\mathbf{r}_i \times \mathbf{s}_i}{|\mathbf{r}_i|^3}\Gamma_i\phi(|\mathbf{r}_i|/\sigma) \tag{9}$$

where $\mathbf{x}_i^1$ and $\mathbf{x}_i^2$ are the end points of a tube, $\mathbf{s}_i = \mathbf{x}_i^2 - \mathbf{x}_i^1$ is an axial vector, $\mathbf{r}_i = \mathbf{x} - \mathbf{x}_i$, $\mathbf{x}_i = (\mathbf{x}_i^1 + \mathbf{x}_i^2)/2$, Γ_i is the circulation, and ϕ is a smoothing function [23] made necessary by the simplicity of the approximation to the Biot–Savart integral that does not take into account the local vortex structure. As in previous studies,

$$\phi(|\mathbf{r}_i|/\sigma) = 1 - (1 - \tfrac{3}{2}(|\mathbf{r}_i|/\sigma)^3)e^{-(|\mathbf{r}_i|/\sigma)^3} \tag{10}$$

where the smoothing parameter σ determines the distance from the center of the tubes within which smoothing takes place. Beyond a distance 2.34σ, $\phi = 1$, and smoothing is not present.

The velocity associated with an individual prism sheet can be determined by the appropriate Biot–Savart integral over its individual volume using the assumption of constant vorticity. By construction, the prisms have a sufficiently high aspect ratio so that it is reasonable to forgo integration in the normal direction in favor of a simple midpoint evaluation. This leaves integration over the triangles themselves, which may be carried out in closed form, though the formulas are lengthy and are not given here. It is also the case that the expense of evaluating the exact relations is such that they are only used for the computation of velocities in the immediate vicinity of any given prism, specifically, within a radius $R_P = 1.5L_T$. At further distances, the sheets are regarded as contributing to the velocity as if they were tubes, and for this purpose their strengths are determined from Eq. (8). It is thus seen that apart from local formulas, the sheets and tubes contribute similarly to the velocity field.

In the boundary element scheme a source strength is determined on each surface triangle such that the sum of contributions produces a potential flow satisfying the nonpenetration boundary condition. The contribution of each triangle is determined by integration of the exact formula, assuming constant source strengths [24]. The latter are determined by iteration using a generalized minimal residual method [25].

The numerical evaluation of the velocity field is carried out using a parallel implementation of the adaptive fast multipole method [26,27] that replaces the nominal $\mathcal{O}(N^2)$ expense of computing the velocities associated with the motion of N vortices via the Biot–Savart law, by a more practical $\mathcal{O}(N)$ cost. As it is currently constituted, parallelization has been implemented fully for the CPU, but not for memory. Generally, for problems of the scale reached in this paper, parallelization is excellent through at least 32 processors.

III. Numerical Problem

The code used in this study is designed for the treatment of flow past arbitrary 3-D smooth bodies and is readily adapted to boundary layers by applying it to the flow past the smooth plate with rounded edges shown in Fig. 3. For sufficiently wide plates, the mean velocities within a region surrounding the center have the high degree of two-dimensionality appropriate to a traditional boundary layer. After some experimentation, a plate with scaled dimensions 1.5 by 2.5 in the streamwise x and spanwise z directions, respectively, and thickness 0.05 in the y direction was adopted. Flow statistics in the subsequent analysis are taken from the middle region $|z| \leq 0.25$ over which there is found to be no noticeable spanwise variation in the mean statistics. As will be seen below, this computational test section is sufficiently large to contain many independent structural features and is comparable in size to that commonly used in grid-based studies using spanwise periodic boundary conditions.

Smooth edges are applied to the plate by affixing semicircular columns on all four sides and quarter-spheres at each of the corners. The incoming flow is in the positive x direction with unit velocity and zero turbulence level. A Reynolds number $R_e = U_\infty L/\nu$ is assigned, where L and U_∞ are the length and velocity scales, respectively, used in scaling the problem.

Though the plate is relatively slender, it is still thick enough to cause some disturbance to the incoming flow that slightly delays the appearance of canonical boundary layers in the streamwise direction. Thinner plates were not used so as to simplify the generation of the triangularization on the plate sides and corners and to avoid the presence of relatively sharp edges.

The surface triangularization used as the basis for setting up the near-wall grid is also shown in Fig. 3. This contains 62,272 triangles with an average length dimension of 0.0114, suggesting that the density of the triangles over the central region ($0 \leq x \leq 1.5$, $|z| \leq 0.25$) is roughly equivalent to having a 44×132 mesh of square grid cells. The mesh of triangular prisms is grown outward automatically from the surface mesh. In all cases considered here, 10 levels of prisms are layered above the initial layer of half-thickness that is adjacent to the boundary.

As mentioned previously, the thickness of the wall mesh is determined consistent with having an aspect ratio of the prisms near 10. Having set this, then a realistic range of Reynolds number will have $\Delta y^+/2 \approx 1.5$. Based on these considerations, two thicknesses for the boundary mesh have been considered here: namely, 0.012 and 0.016, implying that $\Delta y = 0.00126$ and 0.00168, respectively. The average aspect ratios of the prisms for the two cases are then 13.7 and 10.3. For the thinner mesh, a computation with $R_e = 80,000$ is performed, and for the thicker mesh, simulations have been done with $R_e = 30,000$ and 50,000. Each of the computations described here required approximately one week on a SGI Altix 4700 supercomputer at the Pittsburgh Supercomputing Center using 16 processors.

Fig. 3 Plate geometry including surface triangularization. Flow is from left to right (x direction). The normal and spanwise directions are y and z, respectively.

It is within the capabilities of the code used in this study to allow for surfaces that are constructed from several individual pieces, referred to as patches. In fact, the plate in Fig. 3 is made up of 10 patches consisting of the top and bottom flat surfaces, the semicircular curved sides and the four quarter-spherical corners. Any given surface patch is allowed by the software to be regarded as either inviscid or viscous for the purpose of setting boundary conditions. For the inviscid surfaces, only the wall-normal velocity condition is imposed and not the no-slip condition, with the consequence that such surfaces do not produce vorticity.

For the purposes of the present study, in which interest is confined to the flow in the central region, the side curved edges and the four corners are set to be inviscid surfaces thus saving the cost of computing the motion of vortices created in these places. By the same motivation, the rear curved surface at the exit plane is held to be inviscid as well, so that the boundary layers forming upstream separate without vorticity generation on the back rounded surface.

Computations have revealed that the status of the front curved surface (whether viscous or inviscid) has significant consequences for the subsequent downstream flow development. The sensitivity of boundary-layer transition to the geometry of the leading edge is well known [28], and, in particular, a bluff front face tends to produce earlier transition than a more streamlined shape. In the present circumstances, for the viscous blunt front surface a relatively quick transition occurs downstream. In contrast, when this surface is made inviscid it is found that transition is slower to occur and requires a greater distance to develop along the plate. Evidently, this must reflect the absence of vorticity produced upstream of the beginning of the flat surfaces. The subsequent discussion will make clear that the nature of the transition is the same for both cases, though the possibility of having a slower transition is useful for acquiring converged boundary-layer statistics in the Blasius regime as will be evident below. Results from two simulations will be considered in this study: a computation with $R_e = 80,000$ using the viscous front surface that transitions to an extensive turbulent region and a simulation at a lower Reynolds number $R_e = 50,000$ using the inviscid front curved surface that has a long transition region that finally breaks down to turbulence only near the downstream boundary.

IV. Numerical Results

The boundary-layer simulations begin impulsively from initially quiescent conditions by imposing a unit velocity over the flow domain. Figure 4 shows the time history of the number of filaments N_f and number of vortex tubes N_t for the calculation at $R_e = 80,000$, which is representative of other cases as well. In this, the exit plane is held at $x = 1$ until $t = 0.94$ when it is increased to $x = 1.25$. At $t = 1.51$ the exit plane is moved back to the rear end of the plate at $x = 1.5$ for the remainder of the computation. Test calculations suggest that this procedure speeds up the computation by allowing for a relative equilibrium to form upstream and then spread downstream, compared against computing the transition to an equilibrium everywhere at the same time.

Beginning at about $t = 2.2$ the number of vortex elements and filaments stabilizes with approximately $N_f = 2.7 \times 10^6$ and $N_t = 2.2 \times 10^7$ signaling that global equilibrium has been reached. In this instance, production of new tubes at the mesh surface and through vortex stretching is in balance with vortex destruction largely through loop removal and convection through the rear boundary. The average filament contains about 8 vortex tubes in equilibrium. In fact, the filament population contains many with one tube that are relatively recently created and a significant number downstream

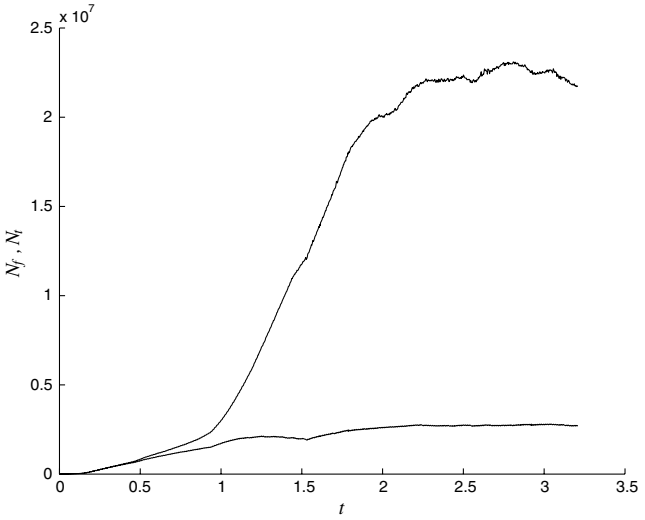

Fig. 4 Variation of N_f (lower curve) and N_t (upper curve) with time.

containing hundreds of tubes. Flow statistics to be presented are based on the data from the start of equilibrium at $t = 2.2$ until the end of the computation at time step 1000, which is at $t = 3.2$, so that the elapsed time for computing averages is 1 dimensionless time unit. This proves to be mostly adequate for predicting the mean flow, but introduces some variability in the higher order statistics such as the Reynolds stresses.

A rendering of the complete vortex field for $0 \leq x \leq 1.5$ as viewed from above at $t = 2.2$ for the higher Reynolds number computation is shown in Fig. 5 and from the side in Fig. 6. The vortex filaments in Fig. 5 are those for which at least one of their component tubes is within $|z| \leq 0.25$, which explains why there is some lateral spread of the vortices beyond $|z| = 0.25$ in the figure. The flow is from left to right and is seen to be initially laminar, then undergoes disturbances leading to a clearly visible vortex structure in a transition region that breaks down into a completely turbulent field on the right. The alignment of vortices in the initial, upstream part of the boundary layer is purely in the spanwise direction. Thus, despite the fact that individual triangles produce separate vortices, the collective motion is entirely smooth as they initially convect along the plate. It may also be noted that there are some small regions barren of vortices. At these locations, intense wallward sweeps of fluid appear to temporarily brush the filaments to the side. In actuality, there is always substantial vorticity in the grid underlying the vortex elements that is not made visible in the figure.

The side view shows the rapid growth of the thickness of the boundary layer after transition. The gap between the vortices and the wall surface near the front of the plate in Fig. 6 gives an indication of where the outer edge of the wall mesh is located. As the flow evolves and becomes turbulent the vortices fill up the region above the plate surface. The figure also reveals the presence of corrugations in the outer edge of the boundary layer that generally represent the footprint of turbulent eddies formed from many individual filaments. This structure is reminiscent of that seen in flow visualizations taken from physical experiments.

In terms of the displacement thickness δ at $x = 0.75$ halfway across the plate, where

$$\delta = \int_0^\infty \left(1 - \frac{\bar{U}}{U_\infty}\right) \mathrm{d}y \tag{11}$$

the computational test section shown in Fig. 5 is approximately 110δ in length and 37δ in width. In terms of the boundary-layer thickness at the exit plane, the width of the region in Fig. 5 is approximately five times this scale. Generally speaking, the extent of the computational domain is of a magnitude similar to or larger than that of other numerical studies that have been performed. Transition in this flow is seen to be before the midpoint of the plate so that an extensive fully turbulent field is available for analysis.

As mentioned previously, the use of an inviscid front curved surface and lower Reynolds number has the effect of reducing perturbations so that transition is significantly delayed. This is evident in the overhead view of the vortex filaments for a simulation with $R_e = 50,000$ in Fig. 7 that should be contrasted with that in Fig. 5. The transition here occupies almost the full length of the plate so that there is just the beginnings of the turbulent field at the right side of the field of view. The first appearance of structure in the transition is plainly visible just beyond the midpoint of the figure at approximately $x = 0.85$.

A. Flow Statistics

The finite thickness of the plate causes some substantial flow distortion in the vicinity of the leading edge. For the $R_e = 50,000$ simulation this is illustrated in Fig. 8, showing the spanwise-averaged streamwise velocity profiles at several x positions plotted with respect to y/δ. It is seen in the figure that there is an overshoot in the streamwise velocity that gradually dies out with distance along the plate, entirely disappearing by $x = 0.675$. In fact, a closer look at the velocity field shows that there is an approximately 3% enhancement to the freestream velocity outside of the boundary layer that persists along the length of the plate. The overshoot at the leading edge is much reduced for the viscous front surface and is not evident beyond $x \approx 0.2$. Moreover, the external streamwise flow outside the turbulent wall region in the $R_e = 80,000$ simulation is raised to approximately 1.04 along the length of the plate.

Beyond $x = 0.675$ in Fig. 7, in which the effect of the front end distortion is no longer felt until the clear onset of transition at $x = 0.85$ it is appropriate to compare the computed solution to that of the Blasius boundary layer. In fact, Fig. 9 containing a comparison of the computed streamwise velocity and the Blasius profile at $x = 0.675$, shows that the vortex solution does have the

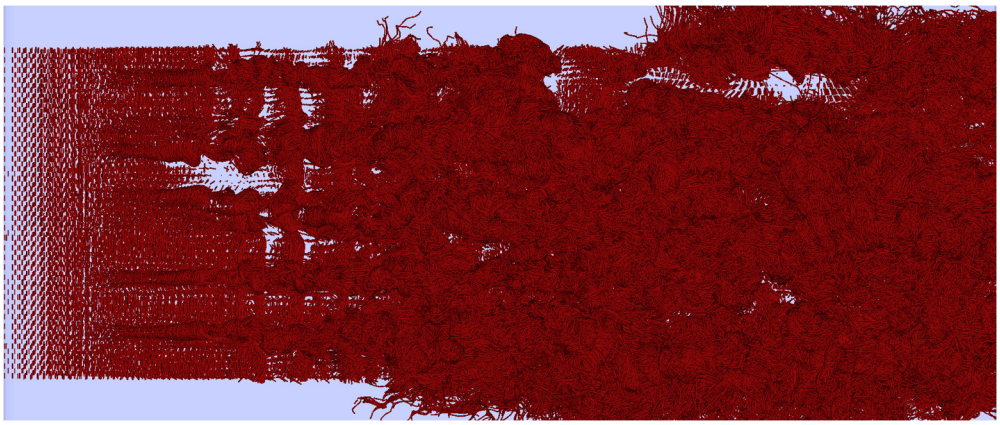

Fig. 5 View from above of the vortex elements for the $R_e = 80,000$ simulation with viscous front boundary.

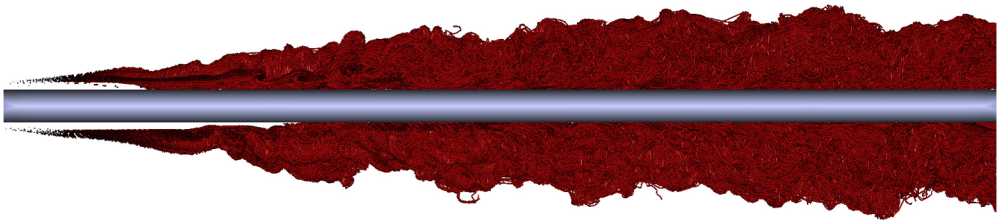

Fig. 6 Side view of the vortex elements for the $R_e = 80,000$ simulation with viscous front boundary.

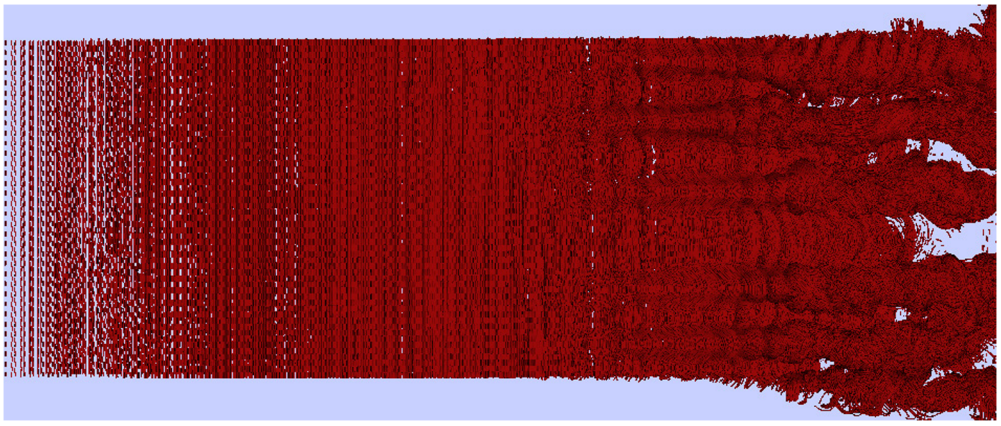

Fig. 7 View from above of the vortex elements in the plate flow with inviscid front boundary.

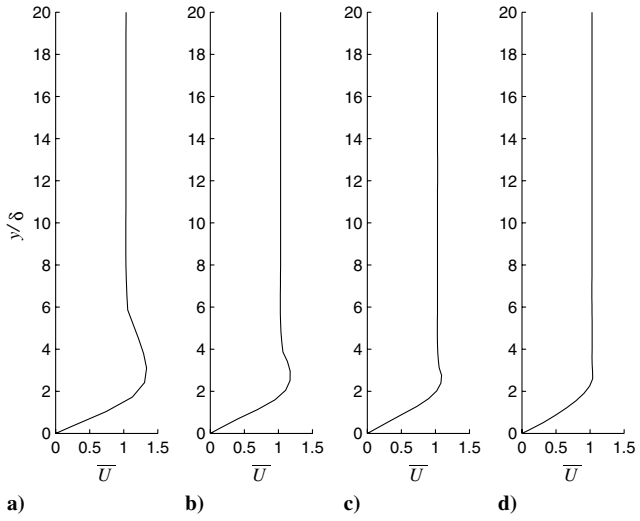

Fig. 8 Streamwise velocity for $R_e = 50,000$ simulation with inviscid leading edge: a) $x = 0.225$, b) $x = 0.375$, c) $x = 0.525$, and d) $x = 0.675$.

characteristics of the Blasius similarity velocity field. In this result, an empirically determined virtual origin of $x = 0.25$ is used in the definition of the similarity variable $\eta = y\sqrt{R_e/(x - 0.25)}$. As is the case in other simulations [16], this is necessary when there is some ambiguity inherent in the determination of a leading edge for the boundary layer. The close agreement with the Blasius velocity field in Fig. 9 holds up until $x \approx 0.85$, where the transitional structures begin to dominate the physics of the flow.

Another indication of the compatibility with the Blasius boundary layer is given in Fig. 10 comparing the computed momentum thickness

$$\theta = \int_0^\infty \frac{\bar{U}}{U_\infty}\left(1 - \frac{\bar{U}}{U_\infty}\right) \mathrm{d}y \tag{12}$$

to that of the Blasius solution: namely,

$$\theta_b = 0.664 R_e^{-1/2}(x - 0.25)^{1/2} \tag{13}$$

Here, the same virtual origin is used as in Fig. 9. According to Fig. 10, throughout the region in which the Blasius boundary layer exists the agreement between computed and theoretical θ values is excellent. Downstream of $x = 0.85$ as transition is entered, there is a rapid growth in θ beyond that of the Blasius result that is indicative of the thickening of the boundary layer that occurs during the transition to turbulent flow.

A plot in Fig. 11 of the development of the drag coefficient, c_f, along the plate shows the drag crisis as the flow transitions into turbulence. Until $Re_x \equiv R_e x = 42,500$(corresponding to $x = 0.85$, where transition begins) c_f decreases somewhat, in agreement with the Blasius boundary-layer relation $c_f = 1.328/\sqrt{R_e x}$. This is

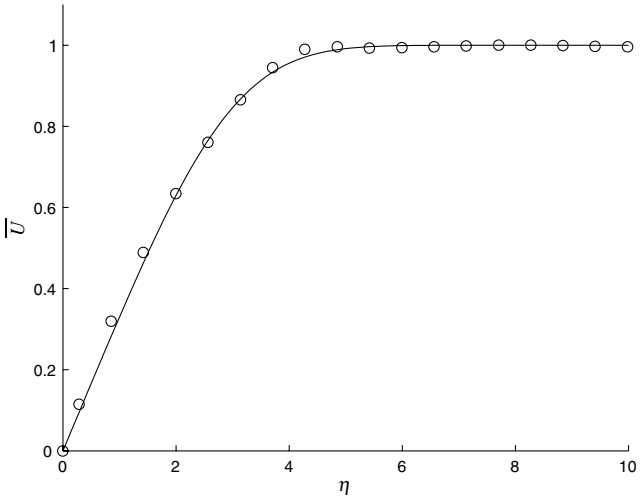

Fig. 9 Velocity in laminar boundary layer; $R_e = 50,000$ simulation at $x = 0.675$ (○) and Blasius velocity profile (line).

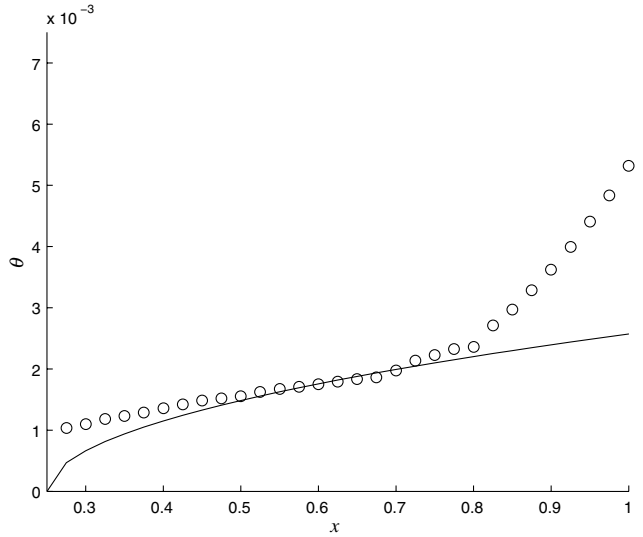

Fig. 10 Momentum thickness in laminar boundary layer: $R_e = 50,000$ simulation (○) and Eq. (13) for Blasius flow (line).

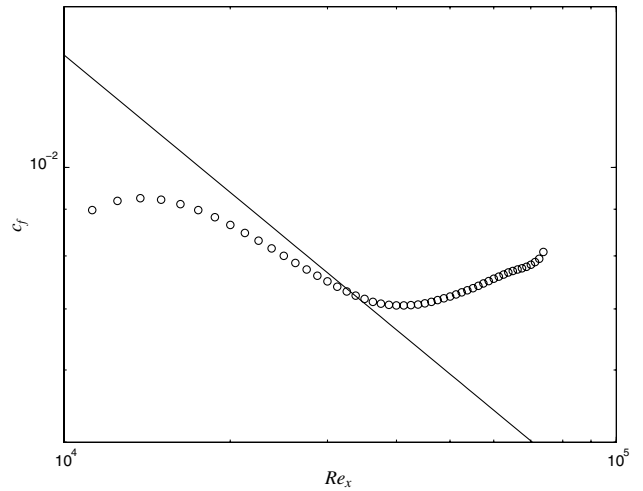

Fig. 11 Drag coefficient computed for $R_e = 50,000$ simulation (○) and $c_f = 1.328/\sqrt{R_e x}$ for Blasius flow (line).

followed by a rise in the drag coefficient as the flow transitions to turbulence. It may be noticed that the values of Re_x are somewhat lower than are ordinarily encountered in a transitioning Blasius boundary layer. This, apparently, reflects the relative coarseness of the vortex element representation that encourages a rapid response to disturbances. The use of greater numbers of vortex elements of lesser strength may counter this tendency. In any case, the fineness of resolution provided in the present study is sufficient for the purposes at hand.

Turning attention now to the $R_e = 80,000$ simulation of the turbulent boundary layer, Fig. 12 gives a plot of the computed trend in $R_\theta = U_\infty \theta/\nu$ along the streamwise extent of the plate that is useful for giving a context to the current simulation in comparison to other studies. It is seen that there is rapid growth in R_θ (or, equivalently, θ) from the leading edge that slows at $x = 0.35$ rising relatively uniformly until $x = 1$, where there is a rapid drop until the end of the plate. The latter effect is a direct result of the relatively crude downstream boundary condition and the presence of an acceleration of the flow over the rear end of the body. The initial part of the boundary layer is strongly affected by the rounded front end so that acceptable data for analysis must come from the central region only. For the purposes of the present study, the turbulent boundary layer between $x = 0.7$ until the peak in R_θ at 1.0 is considered to be a test section used to acquire flow statistics. Velocity data is computed on a

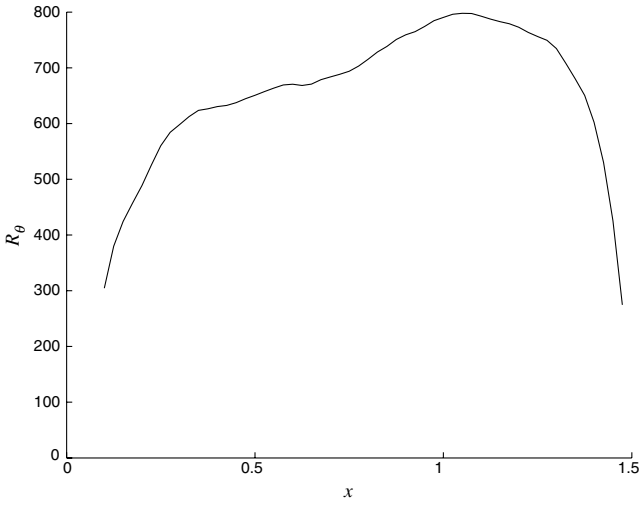

Fig. 12 Variation of R_θ across the plate.

mesh covering this region with averaging done in the spanwise direction at fixed x locations. For most of the following discussion, averaging is expanded to include the data throughout the test section by connecting values using a commonly scaled y coordinate, such as y^+, $y_\delta \equiv y/\delta$, or $y_\theta \equiv y/\theta$. The mean value of R_θ over the test section is 737, and this value will be associated with the flow statistics averaged over the same region.

A traditional semilog plot of the average streamwise velocity scaled in wall units is shown in Fig. 13, together with the mean field at $R_\theta = 670$ computed by Spalart [12]. The slightly larger asymptotic velocity corresponding to $R_\theta = 737$ is consistent with the expected trend. In fact, since the asymptote is U_∞/U_τ and this is related to the local skin-friction coefficient $C_f = 2(U_\tau/U_\infty)^2$, accuracy in the latter is equivalent to accuracy in the former. Below it will be seen that the friction coefficient is well predicted, suggesting that the asymptote in Fig. 13 is also accurately computed. The qualitative agreement with a log-type law and $\bar{U}^+ = y^+$ trend near the wall are also consistent with data. The fitted log law has intercept $B = 5.12$ and von Kármán constant $k = 0.383$ with the fit done by least squares over the region $30 \leq y^+ \leq 80$. These values are within the range of variation seen in experiments [29] and may also possibly reflect the existence of subtle differences between the plate flow and a true zero-pressure-gradient boundary layer.

To enable a more direct comparison with DNS the normalized mean velocity $\bar{U}/\bar{U}_{\max}$ as a function of distance scaled in wall units is

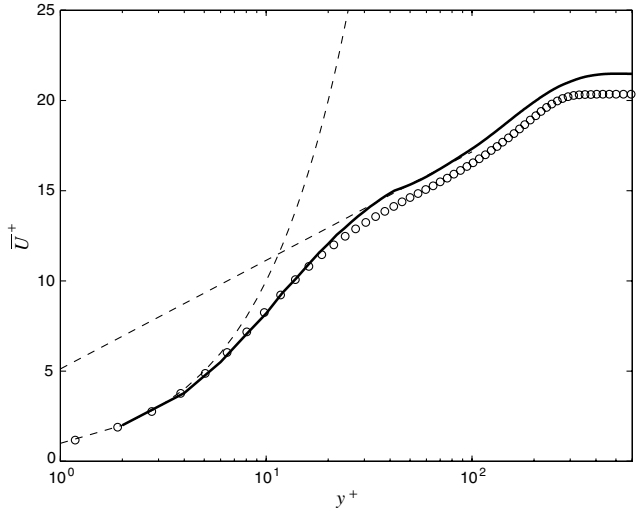

Fig. 13 Semilog plot of $\bar{U}^+$ (solid line) compared to $R_\theta = 670$ DNS solution [12]; $\bar{U}^+ = y^+$ and the fitted log law $\bar{U}^+ = 1/0.383 \log(y^+) + 5.12$ (dashed lines).

plotted in Fig. 14. There is little difference between the present and DNS solutions from this point of view. Two other alternatives for scaling distances in the wall-normal direction are in terms of the displacement thickness δ and the momentum thickness θ. As shown in Fig. 15 the present simulation and the DNS $R_\theta = 670$ solution compare extremely well in these cases also. Overall, the results in these several figures give an indication of the inherent accuracy and physicality of the vortex filament prediction of the mean velocity in the turbulent boundary layer.

Some idea of how the present computation fits in with results from a wider range of experiments is provided by Fig. 16, showing the predicted friction coefficient and the shape factor, which is defined as the ratio δ/θ. The results for the vortex filament calculation are given between the position $x = 0.125$ and 1 over which range R_θ monotonically increases from 380 to 790. In regard to Fig. 16a, below $R_\theta \approx 650$ the friction coefficient angles off toward the Blasius result generally following a trend similar to that reported in other studies [15]. The computed results for $R_\theta > 650$ are within the fully turbulent test section $0.7 \leq x \leq 1$, and for these C_f fits in closely with data taken from a variety of sources. Much the same conclusions can be drawn in the case of the shape factor that is well inside the range of data from other studies in the turbulent regime above $R_\theta = 650$ and branches upward to the laminar flow result below this.

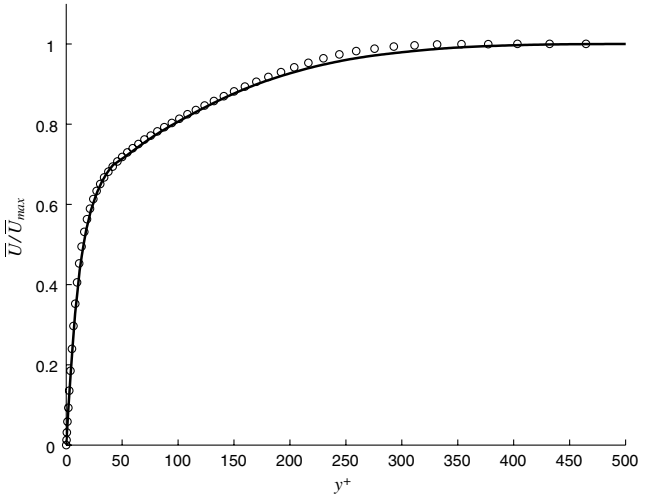

Fig. 14 Comparison of $\bar{U}/\bar{U}_{\max}$ in terms of wall variables; vortex filament scheme (line) and $R_\theta = 670$ DNS solution [12] (○).

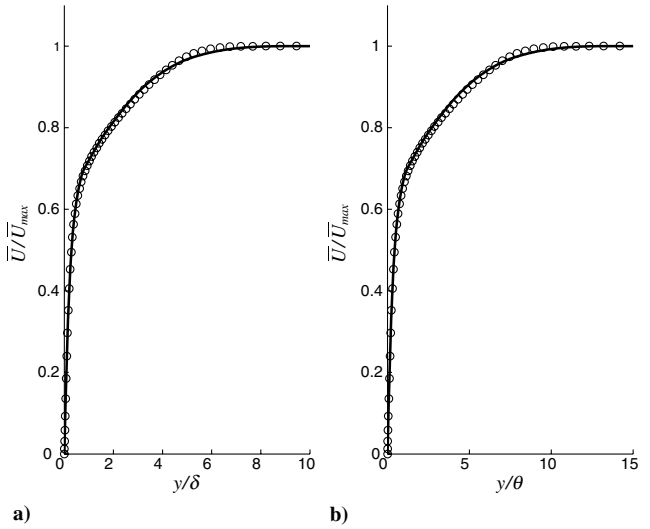

Fig. 15 Variation of $\bar{U}/\bar{U}_{\max}$ with a) y/δ and b) y/θ; vortex filament scheme (line) and $R_\theta = 670$ DNS solution [12] (○).

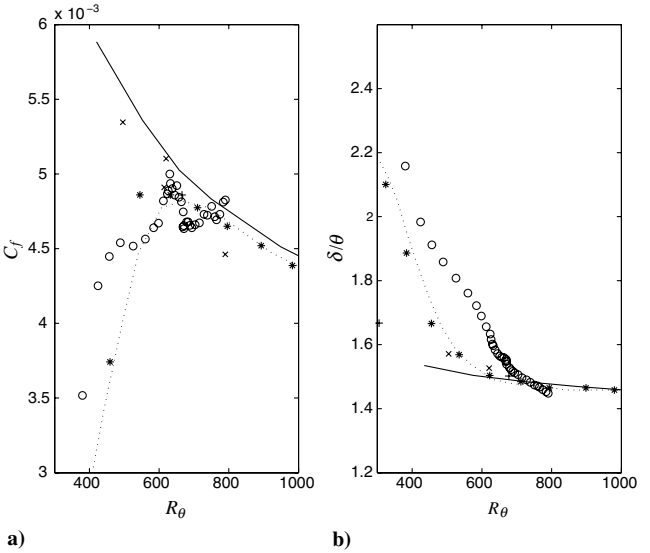

Fig. 16 Plots of a) local skin-friction coefficient and b) shape factor vs R_θ; current simulation with $R_e = 80,000$ (○); DNS [12] (+), DNS [15] (dotted lines), and various experiments [12,37] (solid line, ×, and *).

It should be noted as well that averaging over a longer time interval would likely reduce some of the scatter in the computed results.

Results for the normal Reynolds stresses compared to DNS [12] at $R_\theta = 670$ and 1410 are shown in Fig. 17. These generally have the correct qualitative behavior with the principal exception being the absence of the distinctive peak in streamwise Reynolds stress near the wall. The magnitude of the wall-normal and spanwise Reynolds stresses are somewhat overpredicted, suggesting the need for greater resolution in the wall mesh. In the outer flow, the Reynolds stresses appear to have magnitudes that are more aligned with the $R_\theta = 1410$ computations than the data taken from the simulation with the more similar Reynolds number.

The predicted Reynolds shear stress $\overline{uv}$, shown in Fig. 18a, is seen to have properties consistent with Fig. 17, especially including an overestimation of $\overline{uv}$ that matches that of the normal stresses. The second figure in 18 displays the scaled Reynolds shear stress, which is seen to have some qualitative consistency with DNS, with the greatest distortion showing up next to the wall. The far-field trend in this case follows that of the more appropriate of the two DNS data sets.

As mentioned above, it is likely that the coarseness of the near-wall mesh (for which the dimension $\Delta z^+ \approx 40$) has a primary affect on the Reynolds stress results in Figs. 17 and 18. Other factors possibly

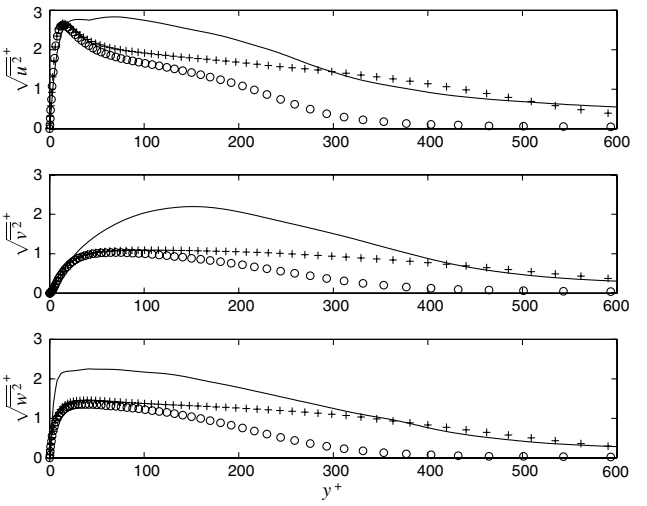

Fig. 17 Normal Reynolds stresses in $R_e = 80,000$ simulation; filament computation (line), DNS [12] $R_\theta = 670$ (○), and DNS [12] $R_\theta = 1410$ (+).

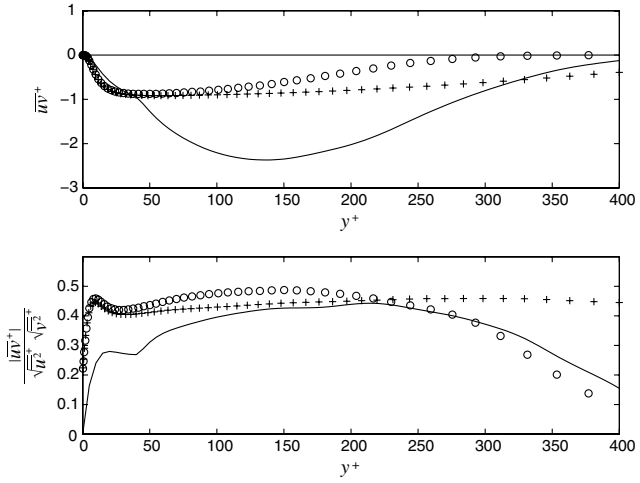

Fig. 18 Reynolds shear stress in $R_e = 80,000$ simulation; filament computation (line), DNS [12] $R_\theta = 670$ (○), and DNS [12] $R_\theta = 1410$ (+).

influencing the comparisons are the relatively short time of the sampling interval and the differences between the plate flow and a zero-pressure-gradient boundary layer including the outward acceleration at the leading edge and the vortex removal at the end of the plate. In this regard, the downstream persistence of disturbances at the front of the plate may be more of a factor for the Reynolds stresses than the mean field itself. An additional consideration that is known to cause some overprediction of the Reynolds stresses [4,5] is the maximum length of the vortex tubes. Though this is kept to the relatively small value of 0.01 in this work, it is still larger than the magnitude of 0.005 that was recommended in an earlier study [4]. It is interesting to note that whatever discrepancies appear with the Reynolds stresses as they have been computed thus far, it does not seem to translate into a noticeable loss of accuracy in computing the mean velocity field. It may be surmised that this is consistent with the observation [29] that from one boundary-layer experiment to another, the Reynolds stresses tend to show a wider range of variability than does the mean velocity.

B. Structural Aspects

Streamwise evolving perturbations in the vortex filament field were seen to be a common and essential aspect of the transition as it was observed in Figs. 5 and 7. A close-up view of two of these structures taken from the lower left of Fig. 5 are shown in Fig. 19. Though not shown here, such structures occur throughout the entire spanwise width of the plate encompassing $|z| \leq 1.25$ as well as at arbitrary times during the simulations. Similar structures are also seen in other computations of bounded flows using the filament scheme in which a transition region is present.

A detailed look at some aspects of the structures will now be given including establishing a connection between these results and previous studies. The earliest sign of transition in the simulations is a gradual undulation into and out of the streamwise direction by the nominally spanwise vortex filaments. A sense of this motion is most visible in Fig. 7 just upstream of the first appearance of the streamwise structures. A similar effect has been observed in a similar place within transition in grid-based simulations in which vortex lines have been reconstructed [20]. Bending of the spanwise vortex filaments into and out of the streamwise direction clearly conforms to the presence of alternating high- and low-speed perturbations in the streamwise velocity associated with the boundary layer. The degree to which vortices are perturbed forward and backward out of the spanwise direction grows with downstream distance. Vortices in this arrangement can induce lift up for the downstream-pointing perturbations and a motion toward the wall for the upstream pointing bends. With the presence of the boundary suppressing the latter it is evident that vortex lift-up is favored, and this process results in the initiation of the streamwise features visible in Figs. 5, 7, and 19.

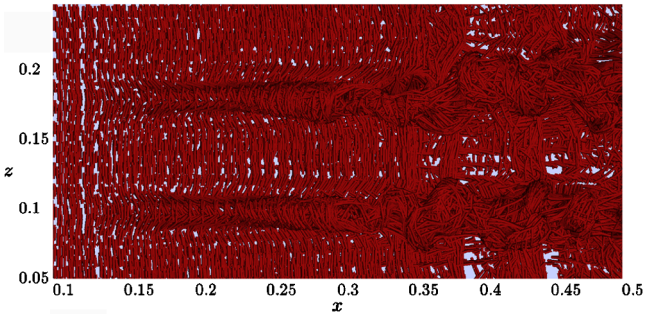

Fig. 19 Vortex furrows in transition and their breakdown into turbulence.

Figure 20 contains end-on views of the vortex filaments intersecting thin regions aligned in the spanwise direction at x locations 0.985 in the $R_e = 50,000$ simulation and 0.18 in the $R_e = 80,000$ simulation, shortly after the initiation of the perturbations. The structures visible in the overhead views match exactly with those in Fig. 20 so that the former clearly represent lifted up vortices forming raised furrows or creases in the surface vortex field. For the larger R_e it may be noticed that the scale of the lifted regions is reduced.

The furrowlike arrangements of vortex filaments overlie low-speed streaks in the transitioning boundary layer as may be seen in Fig. 21, showing contours of streamwise velocity on the plane $y = 0.0076$ (corresponding to $y^+ \approx 22$) for the same field of view as in Fig. 7. The low-speed streaks in the former figure coincide with the streamwise structures in the latter and a similar result holds for the vortex field in Fig. 5. The streaks in Fig. 21 are of a form and separation equivalent to those observed under a relatively wide set of circumstances [15,17,20,28,30]. In particular, the spacing of the streaks or, equivalently, the vortex furrows is on the order of the boundary-layer thickness (approximately 0.1 in this calculation) and thus in agreement with general observations about the properties of streaks in boundary layers [15,28]. It is clear from this that the transition mode found here is of the Klebanoff type [16], which includes low-speed streaks with their accompanying vortical structure that breaks down into turbulence. The streaks in Fig. 21 extend downstream to well within the region in which the raised sections of vorticity have evolved to a more or less chaotic state.

At the onset of the furrows, the lifted vorticity can be expected to be tilted forward by the faster-moving outer flow, and this is plainly evident in Fig. 22, which contains a 3-D view of the filaments in this location. Associated with the raised and forward tilted filaments is counter-rotating motion if viewed in transverse planes, as illustrated in Fig. 23. Here, vortex filaments intersecting a narrow region around $x = 0.30$ for the $R_e = 80,000$ simulation are superimposed upon a

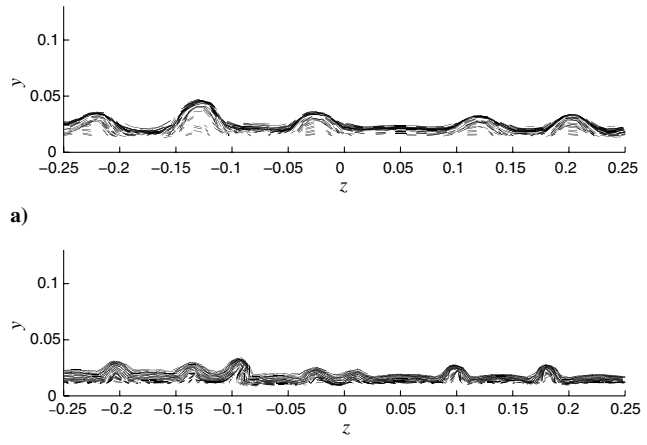

Fig. 20 Vortex tubes that intersect narrow spanwise cuts: a) $R_e = 50,000$ simulation at $x = 0.985$ and b) $R_e = 80,000$ simulation at $x = 0.18$.

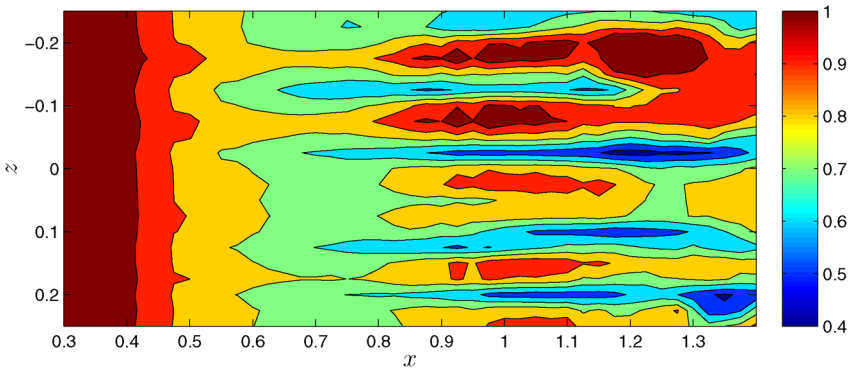

Fig. 21 Contours of streamwise velocity on plane $y = 0.0076$ corresponding to $y^+ \approx 22$.

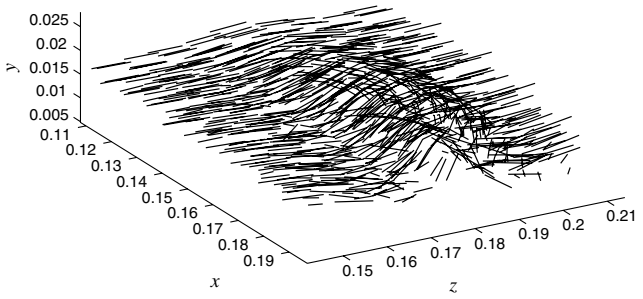

Fig. 22 Forward-tilting vortex filaments forming furrows in early transition.

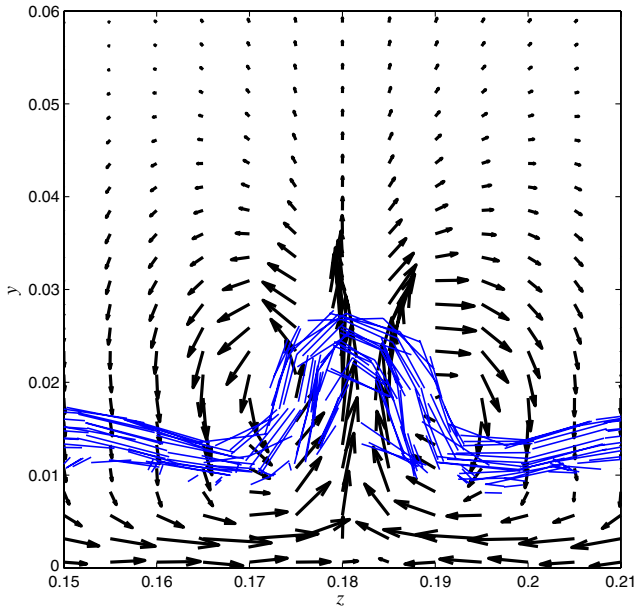

Fig. 23 Vortex tubes that intersect a narrow spanwise cut at $x = 0.18$ with superimposed velocity vectors.

quiver plot of velocity vectors. This flowfield focuses slow-moving fluid that is adjacent to the wall into a position underneath the furrow and, as will be shown below, ejects it up through the center. It should be noted that although there is counter-rotating motion, this is not caused by structural elements in the form of streamwise vortices. An observation very similar to this has been made by Sheng et al. [31] using measured velocities taken by digital holographic microscopy for which they calculated vortex lines in the vicinity of local stress maxima associated with counter-rotating motion in the turbulent flow region.

Downstream, the form of the vortex furrows changes in which the lifted up vorticity appears to gain more autonomy from the vortex layer covering the surface. In this progression, the cross sections of the furrows take on a mushroom shape, as shown for both the high- and low-Reynolds-number simulations in Fig. 24. The views here are downstream of the corresponding images in Fig. 20. These pictures have much in common with smoke visualizations [32] of the boundary-layer structure. As before, the scale of the structures is larger for the lower Reynolds number case. The appearance of the mushrooms corresponds with the completion of the vortex tilting process, leaving some of the filaments with a purely streamwise orientation. Such filaments concentrate in the lobes of the mushrooms and are now detached from the wall surface, as illustrated in Fig. 25, showing a detailed 3-D view of the filaments composing one of the furrows in Fig. 19, in which it has acquired the mushroom shape. Specially highlighted in this figure are vortex tubes with a pronounced streamwise orientation. These are seen to populate mainly the lobes of the mushrooms as they form a true counter-rotating pair of vortices. The latter point is made clear in Fig. 26, in which a velocity quiver plot is overlaid on a cross section of the filaments forming a mushroom shape. It is especially interesting to note how the appearance of the detached streamwise vortex pair appears to occur simultaneously with the pulling together of the sides of what was initially the simple furrows depicted in Fig. 20 and that has now become the narrow, almost vertical stems of vorticity being lifted away from the wall into the mushrooms. Evidently, the detached streamwise vortices drive the shape and evolution of the furrow at this time. The ejected vortex filaments rising in the stem merge into the shear layers formed across the tops of the structures. Similar behavior appears to occur in all the furrows that were observed in the present simulations, though there is variations from one to another, as seen in Fig. 24, reflecting to some extent interactions with other nearby structures.

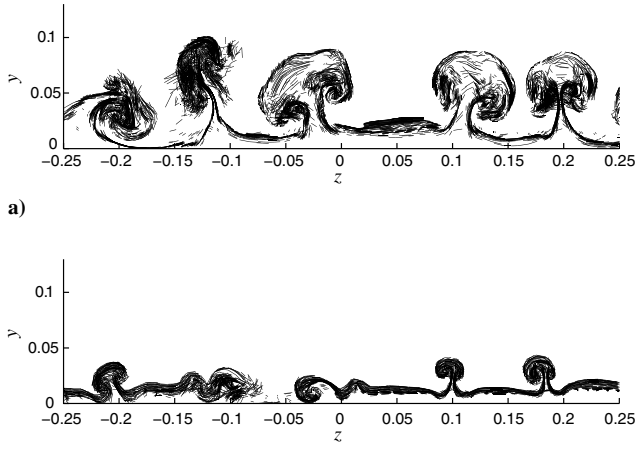

Fig. 24 Vortex tubes that intersect narrow spanwise cuts: a) $Re = 50,000$ simulation at $x = 1.2$ and b) $R_e = 80,000$ simulation at $x = 0.3$.

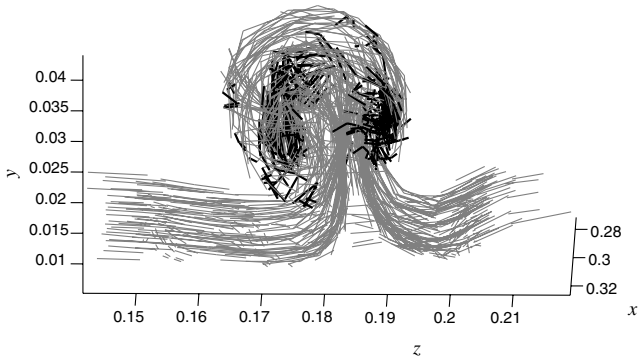

Fig. 25 Three-dimensional view of vortex filaments forming a mushroom shape. Dark lines are streamwise-oriented filaments.

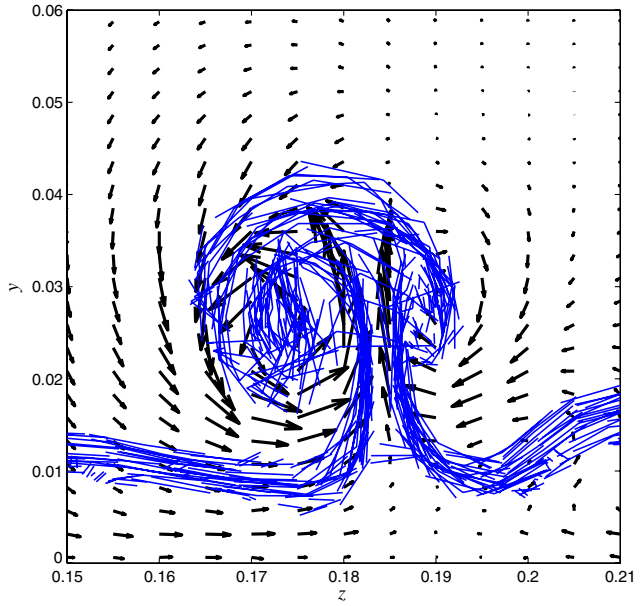

Fig. 26 Vortex tubes that intersect a narrow spanwise cut at $x = 0.3$ with superimposed velocity vectors.

The maturing of the furrows into the detached mushroom-shaped structures appears to be accompanied by ejection of low-speed fluid from away from the wall. This is illustrated in Figs. 27–29, providing views of the streamwise velocity contours accompanied by projections of the local vortex filaments on cross planes intersecting a particular furrow. In the first image, the furrow is a simple perturbation in the spanwise vorticity field, and in the last image, a mushroom-shaped form is present. Figure 28 is a middle point at which the low-speed fluid first gathered by the furrow begins to lift up as the mushroom is just beginning to form. When the mushroom is present, the low-momentum fluid is detached completely from the wall. To a stationary observer it can be imagined that this sequence of events has all the characteristics of the ejection process that feeds into the Reynolds shear stress.

As mentioned previously, it is evident from Figs. 5 and 7 that there is a tendency in the simulations for the vortex filaments to roll up, forming noticeable spanwise structures. Figure 7 suggests that the process can start early in transition though there is great latitude in where and to what extent it occurs. For example, multiple furrows may be affected simultaneously by roll-up, but not in all cases. The roll-up mechanism thus also contributes to the individuality by which each furrow evolves into turbulence. The idea that roll-up contributes to the presence of arch vortices is widely accepted [19,33] and is consistent with this study. The coalescence of vortex filaments to form a group of three such arched structures for the simulation at $R_e = 50,000$ is shown in Fig. 30. These are located on the second

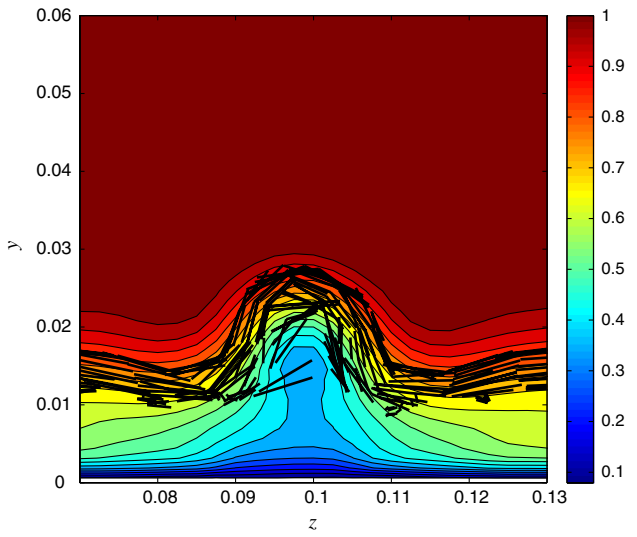

Fig. 27 Streamwise velocity contours and vortex filaments at $x = 0.2$ for $R_e = 80,000$ simulation.

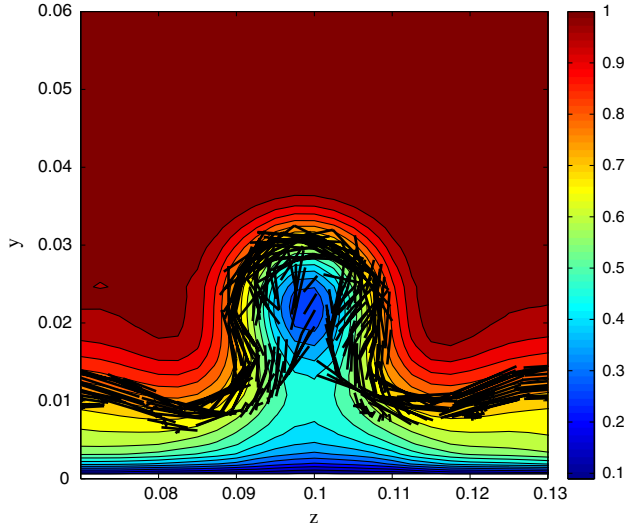

Fig. 28 Streamwise velocity contours and vortex filaments at $x = 0.25$ for $R_e = 80,000$ simulation.

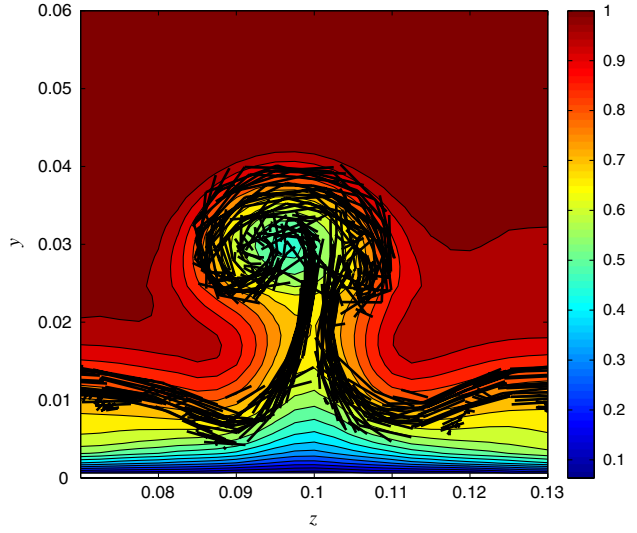

Fig. 29 Streamwise velocity contours and vortex filaments at $x = 0.3$ for $R_e = 80,000$ simulation.

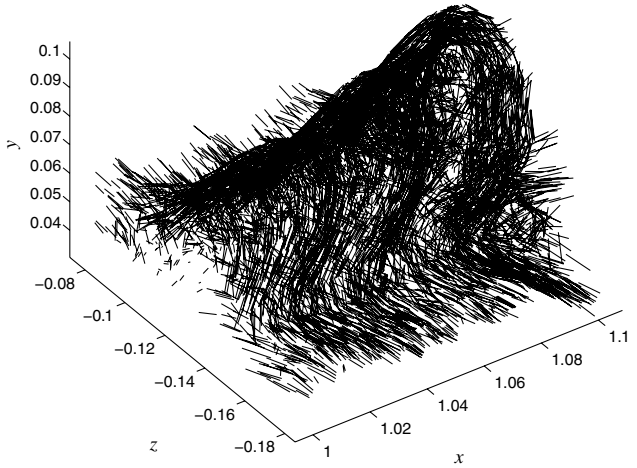

Fig. 30 Close-up 3-D view of vortex filaments revealing arch vortices.

streamwise perturbation from the top shown in Fig. 7 and are representative of the vortex roll-up as it affects the furrows throughout the field. The arched structures in Fig. 30 straddle the furrow with the vortex filaments in this location spreading laterally at the edge. Further downstream, more complicated patterns can form such as when vortex roll-up is simultaneous with the formation of the mushroom-shaped vortices. In the final stages of breakdown vortex filaments in the furrows can be found to also wrap around the rolled-up vortices. In this, as well as the general layout of the vortices, there appears to be some qualitative affinity with the structure of free shear layers and jets wherein systems of roller and rib vortices form.

C. Comparison with Previous Results

Investigation of the boundary-layer structure using experimental and computational techniques has led to a number of specific conclusions concerning its character, such as the existence of hairpin vortices that may be compared and contrasted with the results of the filament simulation. It is apparent from the previous discussion that coherent vortices are identified in the filament computations via direct observation and this may be contrasted with the common need in grid-based simulations to incorporate a protocol for extracting structure from the simulated results. This difference is a consequence of the fact that the vortex filaments supply information about the orientation and concentration of the vorticity that is not evident in the vorticity field itself.

The commonly deployed vortex identification strategies are based on the assumption that regions of rotational motion are synonymous with the actual structure in the flow. Typically, such scalar fields as the negative isosurfaces of the middle eigenvalue λ_2 of the matrix $S^2 + W^2$ (where S and W are, respectively, the symmetric and anti-symmetric parts of the velocity gradient tensor $\nabla\mathbf{U}$) are used to mark the physical form of structures. Negative values of λ_2 correlate with regions of low pressure that mark rotational motion [34]. In most cases, the same kinds of structures that are identified by λ_2 are also found by the use of alternative methods [2].

It is generally understood that for the Klebanoff-type transition seen here, low-speed streaks form within the streamwise legs of Λ-shaped vortices. Further downstream the structures are commonly described as hairpinlike vortices occurring either alone or in nested groups forming packets. Other terms for these vortices are horseshoe or, possibly, omega-shaped hairpins or Ω vortices; these names are used interchangeably here. Further evolution of the boundary-layer disturbances, may include the appearance of additional kinds of structures [33], such as vortex rings, chains of ringlike vortices, and solitonlike coherent structures. The present discussion concentrates on the early to middle stages of transition when the structures are most clearly observed, free of mutual interactions.

The vortex furrows that represent the dominant structural observation of the present simulations may be connected to past results by computing their associated λ_2 isosurfaces. This result is shown in Fig. 31, in which it is seen that for the two structures in Fig. 19, the eigenvalue method identifies regions of rotational motion in the form of the expected Λ or hairpin vortices. Note that the image in this figure is qualitatively the same under a wide range of numerical values used to define the isosurface. To make the relationship of these regions with the past figures more precise, Fig. 32 shows intersections of the isosurfaces in Fig. 31 with spanwise planes including the velocity vector plots. The first of these, Fig. 32a, makes it clear that the rotational motion corresponding to λ_2 in this case is the same as was seen in Fig. 23, in which it was noted, as in Fig. 22, that the filaments are not organized to form a true streamwise vortex pair.

A similar comparison in Fig. 32b shows that the vortex pair within the detached mushroom-shaped structure that was noted previously in Figs. 25 and 26 corresponds to the isosurfaces selected by λ_2 in Fig. 31. This means that in this region the "legs" of the hairpin vortex pictured in Fig. 31 are truly associated with the distribution of streamwise vortex filaments in the raised furrow. Thus, when the mushroom shape forms, the legs of hairpins are truly representing vortical structures in the flow, though to be accurate they are but one part of a more complex structure.

The vortex arches that appear to connect the leg vortices depicted in Fig. 31 are locations at which spanwise-oriented vortex filaments have rolled up. This connection is firmed up in Fig. 33, in which the isosurface of constant λ_2 is plotted for the same scene as was shown in Fig. 30. It is clear that vortex arches identified by regions of rotational motion do correspond to actual arches formed from filaments. However, examination of the complete filament field does not support the idea that the arches together with the two leg vortices form a self-contained hairpinlike structure. For example, as in Fig. 30, it cannot be said that vortex filaments forming the arches directly reorient to form counter-rotating leg vortices. A more precise description appears to be that within the context of a particular vortex furrow, the rotational motion that has the appearance of leg vortices

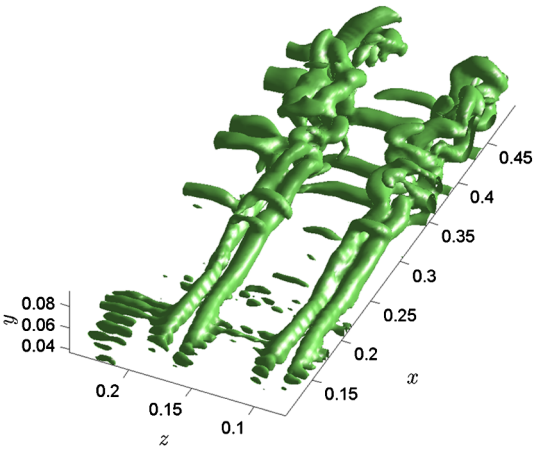

Fig. 31 Isosurfaces of the middle eigenvalue $\lambda_2 = -40$.

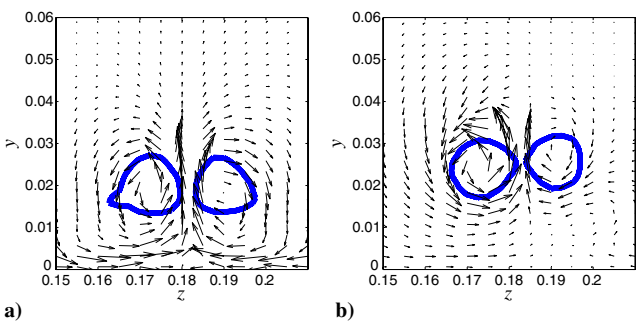

Fig. 32 Quiver plot of velocity with superimposed contours of $\lambda_2 = -40$: a) $x = 0.18$ and b) $x = 0.3$.

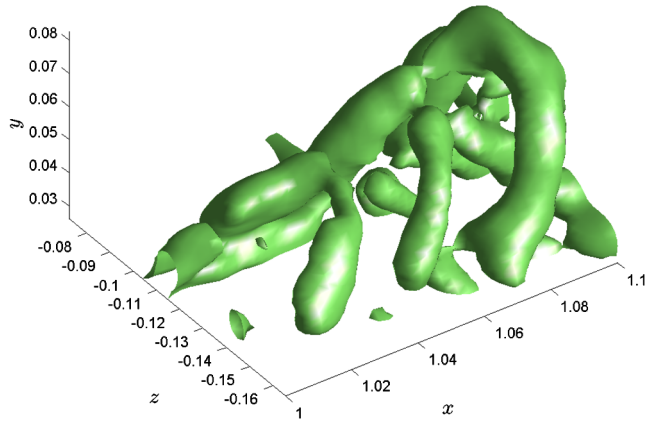

Fig. 33 Isosurfaces of the middle eigenvalue of $S^2 + W^2$ equal to -40.

will have a relationship with the rolled-up arch vortices that are part of the same structure.

The view of the boundary-layer physics in the Klebanoff mode of transition that emerges from the filament simulation may be summarized as consisting of the appearance and subsequent downstream development of furrowlike creases in the vortex field over solid surfaces. Accompanying raised vortices is a tendency to form spanwise-oriented rolled-up vortices. The late stages in the evolution of the furrows include ejected mushroom-shaped vortices with strong interactions with the spanwise structures. While rotations with the characteristics of hairpin vortices are found to be intimately involved with the dynamics of the furrows they do not appear to exist as structural entities in their own right.

The previous discussion suggests that there may be some advantage to understanding the stability of the boundary layer and its transition to turbulence through consideration of the properties of a deforming vortex sheet over a solid surface. This may provide a cohesiveness to the discussion that is difficult to achieve via analysis of structural elements whose precise form is a matter of subjective interpretation. To some extent, such a new approach is more in line with the common description of shear layers and jets in terms of their vortex behavior. It should be noted that some steps toward analyzing the stability of boundary layers through vortex sheets have been made previously [35]. In particular, the stability of a streamwise corrugated vortex sheet (with some similarity to the central region of Fig. 7) has been considered. This has predicted the appearance of streamwise vorticity within the evolving sheet. A next step may be to consider the further stability of the streamwise deformations within the sheet that grow with downstream distance and form the mushroom-shaped vortices. This view may be contrasted with the current practice of directly considering the stability of the streaks themselves [30,36].

V. Conclusions

A grid-free vortex filament scheme conjoined with a grid-based approach in the near-wall region to accurately capture the production of new filaments has been developed with a view toward efficiently and accurately accounting for the physics of turbulent flow in the context of a large eddy simulation. Vortex filaments offer a succinct means of representing essential turbulent vortical structure away from boundaries with minimal numerical diffusion and with the opportunity to incorporate loop removal as a physically motivated subgrid model for regulating energy flow between large and small scales. The finite difference and finite volume scheme used for solving the full viscous flow equations on a thin boundary mesh supplies new filaments to the calculation while respecting the need for high resolution in the wall region in which the idea of a LES is suspect.

The simulations of transitional and turbulent boundary layers described here suggest that beyond agreeing with prior studies in a number of basic flow statistics, the filament methodology has the advantage of providing a somewhat more holistic view of the structural elements of the vorticity field than has generally been possible with other techniques. From this has come an apparent need to reinterpret the meaning of some of the prominent structural aspects of transition that have been identified to date. The essential difficulty heretofore has been the questionable assumption that regions of rotational motion correspond to actual structure. In fact, for the Klebanoff mode of transition that was investigated here wherein low-speed streaks form, it was seen that the streaks are produced by raised furrows in the vortex sheet covering the boundary layer that evolve into a mushroom shape with downstream distance. Such vortical objects are seen to generate a rotational field with the appearance of hairpin vortices such as are commonly found in other studies. At their upstream ends, the apparent legs of the hairpins are generated by tilted filaments in the furrows. Downstream, after detachment of the vorticity to produce the mushroom-shaped structures, streamwise vorticity forms within the lobes of the mushrooms that may be considered to be bona fide counter-rotating vortex pairs. Such structure, however, is but one part of the greater whole that consists of a narrow stem of upwelling vorticity from the wall and a broad shear layer of spanwise vorticity across the top. Roll-up of spanwise vorticity occurs potentially at many points along the raised vorticity.

While the structural details of the fully turbulent region were not studied in this work, nonetheless, it is likely that much of what has been seen for transition will apply in this context as well. For example, just as low-speed streaks are produced by a continuous distribution of vorticity in a furrow (compared against a concentrated localized vortical structure) so too it may be that low-speed streaks in the turbulent field are the result of distributed vortical features formed along furrowlike upwellings. According to the results of this study, some indication of the presence of the latter may be implicit in the observation of hairpin packets in numerical computations and physical experiments. Beyond these considerations, there may be advantages to investigating the stability of the boundary layer directly in terms of the properties of the wall-layer vortex sheet. In particular, the stability of the raised vorticity forming furrows should be relevant to understanding the occurrence of streak breakdown and the last stages of transition leading to turbulent flow. One may also move beyond the mode of transition observed in this work to speculate that processes similar to those described here also underlie the local behavior of turbulent spots. These and similar questions will be pursued in further studies.

Acknowledgments

This research was supported in part by the National Science Foundation through TeraGrid resources provided by the Pittsburgh Supercomputing Center.

References

[1] Bernard, P. S., and Wallace, J. M., *Turbulent Flow: Analysis, Measurement and Prediction*, Wiley, Hoboken, NJ, 2002.

[2] Chakraborty, P., Balachandar, S., and Adrian, R. J., "On the Relationships Between Local Vortex Identification Schemes," *Journal of Fluid Mechanics*, Vol. 535, 2005, pp. 189–214. doi:10.1017/S0022112005004726

[3] Schafhitzel, T., Baysal, K., Rist, U., Weiskopf, D., and Ertl, T., "Particle-Based Vortex Core Line Tracking Taking into Account Vortex Dynamics," *ISFV13—13th International Symposium on Flow Visualization*, Nice, France, 2008.

[4] Bernard, P. S., "Gridfree Simulation of the Spatially Growing Mixing Layer," *AIAA Journal*, Vol. 46, No. 7, 2008, pp. 1725–1737. doi:10.2514/1.34205

[5] Bernard, P. S., "Vortex Filament Simulation of the Turbulent Coflowing Jet," *Physics of Fluids*, Vol. 21, 2009, Paper 025107. doi:10.1063/1.3081559

[6] Kravchenko, A. G., and Moin, P., "On the Effect of Numerical Errors in Large Eddy Simulations of Turbulent Flows," *Journal of Computational Physics* Vol. 131, No. 2, 1997, pp. 310–322. doi:10.1006/jcph.1996.5597

[7] Moin, P., "Numerical and Physical Issues in Large Eddy Simulation of Turbulent Flows," *JSME International Journal, Series B (Fluids and Thermal Engineering)*, Vol. 41, 1998, pp. 454–463.

[8] Sagaut, P., *Large Eddy Simulation for Incompressible Flows: An Introduction*, 3rd ed., Springer–Verlag, New York, 2005.
[9] Bernard, P. S., "Turbulent Flow Properties of Large Scale Vortex Systems," *Proceedings of the National Academy of Sciences of the United States of America*, Vol. 103, No. 27, 2006, pp. 10174–10179. doi:10.1073/pnas.0604159103
[10] Chorin, A. J., "Hairpin Removal in Vortex Interactions II," *Journal of Computational Physics*, Vol. 107, No. 1, 1993, pp. 1–9. doi:10.1006/jcph.1993.1120
[11] Chorin, A. J., *Vorticity and Turbulence*, Springer–Verlag, New York, 1994.
[12] Spalart, P. R., "Direct Simulation of a Turbulent Boundary Layer up to $R_\theta = 1410$," *Journal of Fluid Mechanics*, Vol. 187, 1988, pp. 61–98. doi:10.1017/S0022112088000345
[13] Rai, M. M., and Moin, P., "Direct Simulations of Transition and Turbulence in a Spatially Evolving Boundary Layer," *Journal of Computational Physics*, Vol. 109, No. 2, 1993, pp. 169–192. doi:10.1006/jcph.1993.1210
[14] Rist, U., and Fasel, H., "Direct Numerical Simulation of Controlled Transition in a Flat-Plate Boundary Layer," *Journal of Fluid Mechanics*, Vol. 298, 1995, pp. 211–248. doi:10.1017/S0022112095003284
[15] Jacobs, R. G., and Durbin, P. A., "Simulations of Bypass Transition," *Journal of Fluid Mechanics*, Vol. 428, 2001, pp. 185–212. doi:10.1017/S0022112000002469
[16] Bake, S., Meyer, D. G. W., and Rist, U., "Turbulence Mechanism in Klebanoff Transition: A Quantitative Comparison of Experiment and Direct Numerical Simulation," *Journal of Fluid Mechanics*, Vol. 459, 2002, pp. 217–243. doi:10.1017/S0022112002007954
[17] Ovchinnikov, V., Choudhari, M. M., and Piomelli, U., "Numerical Simulations of Boundary-Layer Bypass Transition Due to High-Amplitude Free-Stream Turbulence," *Journal of Fluid Mechanics*, Vol. 613, 2008, pp. 135–169. doi:10.1017/S0022112008003017
[18] Wu, X., and Moin, P., "Direct Numerical Simulation of Turbulence in a Nominally Zero-Pressure-Gradient Flat-Plate Boundary Layer," *Journal of Fluid Mechanics*, Vol. 630, 2009, pp. 5–41. doi:10.1017/S0022112009006624
[19] Zhou, J., Adrian, R. J., Balachandar, S., and Kendall, T. M., "Mechanisms For Generating Coherent Packets of Hairpin Vortices," *Journal of Fluid Mechanics*, Vol. 387, 1999, pp. 353–396. doi:10.1017/S002211209900467X
[20] Ducros, F., Comte, P., and Lesieur, M., "Large-eddy Simulation of Transition to Turbulence in a Boundary Layer Developing Spatially over a Flat Plate," *Journal of Fluid Mechanics*, Vol. 326, 1996, pp. 1–36. doi:10.1017/S0022112096008221
[21] Kawai, S., and Fujii, K., "Compact Scheme with Filtering for Large-Eddy Simulation of Transitional Boundary Layer," *AIAA Journal*, Vol. 46, No. 3, 2008, pp. 690–700. doi:10.2514/1.32239
[22] Bernard, P. S., "A Deterministic Vortex Sheet Method for Boundary Layer Flow," *Journal of Computational Physics*, Vol. 117, No. 1, 1995, pp. 132–145. doi:10.1006/jcph.1995.1051
[23] Puckett, E. G., "Vortex Methods: An Introduction and Survey of Selected Research Topics," *Incompressible Computational Fluid Dynamics: Trends and Advances*, edited by M. D. Gunzburger, and R. A. Nicolaides, Cambridge Univ. Press, Cambridge, England, U.K., 1993, pp. 335–407.
[24] Hess, J. L., and Smith, A. M. O., "Calculation of Potential Flow About Arbitrary Bodies," *Progress in Aeronautical Sciences*, Vol. 8, 1967, pp. 1–138. doi:10.1016/0376-0421(67)90003-6
[25] Saad, Y., and Schultz, M. H., "GMRES: A Generalized Minimal Residual Algorithm for Solving Nonsymmetric Linear Systems," *SIAM Journal on Scientific and Statistical Computing*, Vol. 7, No. 3, 1986, pp. 856–869. doi:10.1137/0907058
[26] Greengard, L., and Rokhlin, V., "A Fast Algorithm for Particle Simulations," *Journal of Computational Physics*, Vol. 73, No. 2, 1987, pp. 325–348. doi:10.1016/0021-9991(87)90140-9
[27] Strickland, J. H., and Baty, R. S., "A Three-Dimensional Fast Solver for Arbitrary Vorton Distributions," Sandia National Lab. Rept. SAND93-1641, Albuquerque, NM, 1994.
[28] Nagarajan, S., Lele, S. K., and Ferziger, J. H., "Leading-Edge Effects in Bypass Transition," *Journal of Fluid Mechanics*, Vol. 572, 2007, pp. 471–504. doi:10.1017/S0022112006001893
[29] Fernholz, H. H., and Finley, P. J., "The Incompressible Zero-Pressure Gradient Turbulent Boundary Layer: An Assessment of the Data," *Progress in Aerospace Sciences*, Vol. 32, No. 4, 1996, pp. 245–311. doi:10.1016/0376-0421(95)00007-0
[30] Andersson, P., Brandt, L., Bottaro, A., and Henningson, D. S., "On the Breakdown of Boundary Layer Streaks," *Journal of Fluid Mechanics*, Vol. 428, 2001, pp. 29–60. doi:10.1017/S0022112000002421
[31] Sheng, J., Malkiel, E., and Katz, J., "Buffer Layer Structures Associated with Extreme Wall Stress Events in a Smooth Wall Turbulent Boundary Layer," *Journal of Fluid Mechanics*, Vol. 633, 2009, pp. 17–60. doi:10.1017/S0022112009006934
[32] Head, M. R., and Bandyopadhyay, P., "New Aspects of Turbulent Boundary-Layer Structure," *Journal of Fluid Mechanics*, Vol. 107, 1981, pp. 297–338. doi:10.1017/S0022112081001791
[33] Lee, C. B., and Wu, J. Z., "Transition in Wall-Bounded Flows," *Applied Mechanics Reviews*, Vol. 61, 2008, Paper 030802.
[34] Jeong, J., and Hussain, F., "On the Identification of a Vortex," *Journal of Fluid Mechanics*, Vol. 285, 1995, pp. 69–94. doi:10.1017/S0022112095000462
[35] Kawahara, G., Jimenez, J., Uhlmann, M., and Pinelli, A., "Linear Instability of a Corrugated Vortex Sheet—A Model for Streak Instability," *Journal of Fluid Mechanics*, Vol. 483, 2003, pp. 315–342. doi:10.1017/S002211200300421X
[36] Hœpffner, J., Brandt, L., and Henningson, D. S., "Transient Growth on Boundary Layer Streaks," *Journal of Fluid Mechanics*, Vol. 537, No. -1, 2005, pp. 91–100. doi:10.1017/S0022112005005203
[37] Roach, P. E., and Brierly, D. H., "The Influence of a Turbulent Freestream on Zero Pressure Gradient Transitional Boundary Layer Development, Part I: Test Cases T3A and T3b," *ERCOFTAC Workshop: Numerical Simulation of Unsteady Flows and Transition to Turbulence*, Cambridge Univ. Press, New York, 1990, pp. 319–347.

A. Tumin
Associate Editor